The evolution of curvature in planar, photoionization-driven heat fronts

H. J. LeFevre,[1, a)] R. P. Drake,[2] and C. C. Kuranz[1]
[1)]*Nuclear Engineering and Radiological Sciences, University of Michigan, Ann Arbor, MI 48109*
[2)]*Climate and Space Sciences and Engineering, University of Michigan, Ann Arbor, MI 48109*

(Dated: 4 August 2022)

Photoionized plasmas are common in astrophysics and cosmology, especially in space near compact objects, and there are effects from photoionization in high-energy-density plasmas due to the large radiation fields present. Photoionized plasmas are an active area of laboratory research and there are currently experiments to study photoionization-supported heat fronts. These photoionization fronts differ from the physics of diffusive radiation waves, commonly called Marshak waves, that are also an active area of research. This work uses a geometric argument to describe the expected evolution of the photoionization front curvature, in a planar geometry. It then compares this curvature to that of a Marshak wave as a method of diagnosing a heat front experiment. It is found that while the curvature of a planar Marshak wave increases in time, it decreases for a photoionization front. A comparison of radiation energy and electron heat fluxes through the container for the heat front propagating medium demonstrates that the geometric argument for the photoionization front curvature is sufficient. This comparison also demonstrates that wall losses are not significant in a photoionization front because the post-front region is very optically thin. A discussion of the implication this work has on material choice in the targets for an experiment follows.

Recently, measuring and understanding the properties of photoionized plasmas has been of particular interest.[1–3] This is an interesting area of plasma physics due to the prevalence of photoionized plasma in astrophysics with examples being black hole accretion disks, circumstellar media around supernovae, stellar nurseries, and the early universe.[2,4–10] To create a photoionized plasma, there must be a transition from an initially cool, or cooler, state to a condition of higher ionization when a photon source reaches the region of interest. The addition of the external radiation source heats the plasma, which leads to an increase in ionization, as a heat front. These photoionization-driven heat fronts are important for understanding the escape fraction of ionizing radiation from the first galaxies during the reionization of the universe.[10–13] It is important to understand the line emission that comes from recombination in these photoionized plasmas because they influence the inferred properties of observed galaxies.[12] Photoionization fronts are also important for understanding circumstellar interactions in supernovae.[6,7,9] Specifically in type IIn and superluminous supernova that have large regions of radiation-heated material and produce narrow line emission from a relatively stationary circumstellar medium (CSM).[14] The limitations in spectral observations of emission from early galaxies and the difficulty of observing the CSM of individual stars leaves room for laboratory experiments to aid in understanding these astrophysical systems. Additionally, no experiment, to the authors' knowledge, has measured a photoionization front,[15] so identifying signatures of these heat fronts is important for developing a laboratory approach to understanding these problems.

These photoionization-driven heat fronts are typically referred to as I-fronts in the astrophysical literature, but experimental publications refer to them as photoionization (PI) fronts. There is significant literature describing these types of heat fronts in astrophysics[16–20] and in laboratory astrophysics experiments[3,15,21,22]. The physical picture of the simplest PI front is an ionizing radiation source propagating through a heated, optically thin region to a front where the colder material upstream of the front rapidly attenuates the radiation. Due to the supersonic nature of this heat front there is no significant mass density change across the front, but there is an increase in the electron density and plasma temperature due the photoionization-deposited energy. How sharp this front is depends on the material, source spectrum, and source flux. If the atoms of the propagating medium have many electrons then it takes more photon mean free paths to reach a limiting ionization potential, the spectrum sets the maximum ionization state, and the source flux determines how many photoionizations can occur in a time δt. The velocity of the supersonic, PI fronts discussed here is less than the speed of light due to the large photoionization cross section, and therefore small photon mean-free-path, at the front. It is important to note that there are additional physics possible in a PI front, such as shock formation,[15] that are not considered here because there should not be significant differences to the planar geometry curvature. These other PI fronts will have significant changes to the velocity.

In order to characterize the physics in a heat front as a PI front, the experimental work in this area has developed two dimensionless numbers using the atomic rate coefficients.[15,22] Each ionization state transition has its own pair of dimensionless numbers. The first, α, is the ratio of recombination from the next, higher ionization state to the photoionization rate into the next ionization state,

$$\alpha = \frac{n_{i+1}}{n_i}\frac{n_e R_{i+1,i}}{\Gamma_{i,i+1}}, \tag{1}$$

where n_i is the number density of the ith ionization state in cm^{-3}, n_e is the electron number density in cm^{-3}, $R_{i+1,i}$ is the recombination rate coefficient in cm^3 s^{-1}, and $\Gamma_{i,i+1} = \int \frac{E_{R,\nu} c}{h\nu}\sigma_\nu d\nu$ is the photoionzation rate in s^{-1}. In the photoion-

[a)]Electronic mail: hjlefe@umich.edu

Facility	Omega-60	Z-Facility
Material	Nitrogen	Nitrogen
Source brightness temperature (eV)	100	60
Number density (cm^{-3})	2×10^{20}	4×10^{19}
Gas Length (mm)	7	13
Source radius (mm)	1	2.5
α	0.1	0.003
β	1	1

TABLE I. This table shows the design parameters for the known experiments that investigate PI fronts with one at the Laboratory for Laser Energetics' Omega laser facility and the other at Sandia National Laboratories' Z-facility.

ization rate, $E_{R,\nu}$ is the frequency-resolved radiation energy density integrated over solid angle in erg cm^{-3}, ν is the radiation frequency in s^{-1}, c is the speed of light in cm s^{-1}, and σ_ν is the frequency-resolved photoionization cross section in cm^2. The recombination rate coefficient can include many processes, and it is typically assumed to be the sum of the three-body recombination, dielectronic recombination, and radiative recombination rate coefficients. For a PI front, α should be much less than one so that photoionization dominates over recombination. The second dimensionless parameter, β, is one plus the ratio of the electron collisional ionization rate to the recombination rate,

$$\beta = 1 + \frac{n_i}{n_{i+1}} \frac{\langle \sigma v \rangle_{i,i+1}}{R_{i+1,i}}, \tag{2}$$

where $\langle \sigma v \rangle_{i,i+1}$ is the electron collisional ionization rate coefficient in cm^3 s^{-1} and the remaining values are the same as in equation 1. The value of β approaches one when the number of ionization events due to electron collisions is significantly less than the number of recombinations. The addition of one to the ratio in equation 2 is a result of calculating the two and three level model for ionization states and this article uses this form to be consistent with the literature.[15,21,22] This means that in order to produce a PI front it is necessary to have both a value of $\alpha << 1$ and $\beta \approx 1$. There are, to the Authors' knowledge, two experiments currently investigating PI fronts. These experiments occur at the Omega laser facility (Omega)[22,23] at the Laboratory for Laser Energetics and the Z-Facility (Z)[3,4] at Sandia National Laboratories, which provide different radiation sources and geometries. The Omega experiments use high-energy lasers to heat a thin gold foil and use the emission from the non-irradiated surface to drive the heat front into a gas cell of nitrogen gas about 0.5 mm away from the source[24,25]. This laser-produced source doesn't fill the entire cross section of the gas cell, which will lead to an initial curvature of the front as it propagates outwards. In the case of a Z experiment, the source is much farther away, about 45 mm, and the source is large enough to fill the whole gas cell cross section. This leads to a more collimated source driving the front, which will produce a flatter initial curvature. Table I provides rough parameters of the above mentioned experiments along with the expected α and β values from the literature.[3,22]

PI fronts are just one type of heat front and photoionization does not support all types of radiation-driven heat fronts. This makes it important to determine signatures of a PI front compared to other types of heat fronts. There has been significant work on the properties of nonlinear, diffusive radiation waves, such as Marshak waves, in theory, computation, and experiment[26–33]. Of particular interest here, is the work of Back *et al.* and Hurricane *et al.* that describes the experimental observation and theory of curvature in planar, supersonic Marshak waves[27–29]. The results of that work show a decrease in the wave front radius of curvature, in planar geometries, as it propagates farther from the driving source. The explanation for this is energy transport through lossy walls that contain the propagating medium for the supersonic Marshak wave. The current work will show that the curvature of a PI front, in a planar geometry, behaves in the opposite manner to a supersonic Marshak wave and this can be a means for distinguishing the two in experiments. Marshak waves require a large optical depth for diffusive transport, while PI fronts require large photoionization cross sections in the cold material, but small opacity behind the front, which means that these two phenomena are not likely to occur in the same medium. However, this work is a powerful result because it allows an experiment to discriminate between physical processes in heat fronts without the need to make complex measurements of opacities or atomic rate coefficients or for the analysis to rely on sophisticated simulations.

This article begins with motivation and the goals of the work and follows with the geometry of an arbitrary point above a finite disk emitter. Integrating over this geometry provides an expected curvature for the Omega and Z experiments based on an analysis of the average path length above the source. It concludes with an assessment of the effects of energy loss through the container walls in a PI front followed by a discussion and conclusions.

Since the PI front creates an optically thin region behind the front, the radiation streams through this material. This means that the geometry of the source and propagating medium is what drives the curvature of the front. Therefore, a PI front should reach locations of equal path length from the source at the same time, in a homogeneous and isotropic medium.

To determine the path length from the source to an arbitrary point in space, this analysis uses a disk of radius R. Figure 1 shows the geometry of a point in space, $P = P(r, \psi, z)$, above a finite disk and the top-down projection to a two-dimensional plane as well as the variables used to describe the path length to P. The top-down projection in Figure 1 b allows for the calculation of distance from a point on the source, u, to the projected point P', called l', which then makes the total path length $l = l(\beta, w) = \sqrt{l'^2 + z^2}$, where z is the height above the projection plane. The description of the distance between any point on a disk and a point P is,

$$l = \sqrt{w^2 + r^2 - 2wr\cos\beta + z^2}, \tag{3}$$

where w is the distance from the origin, o, to the point on the

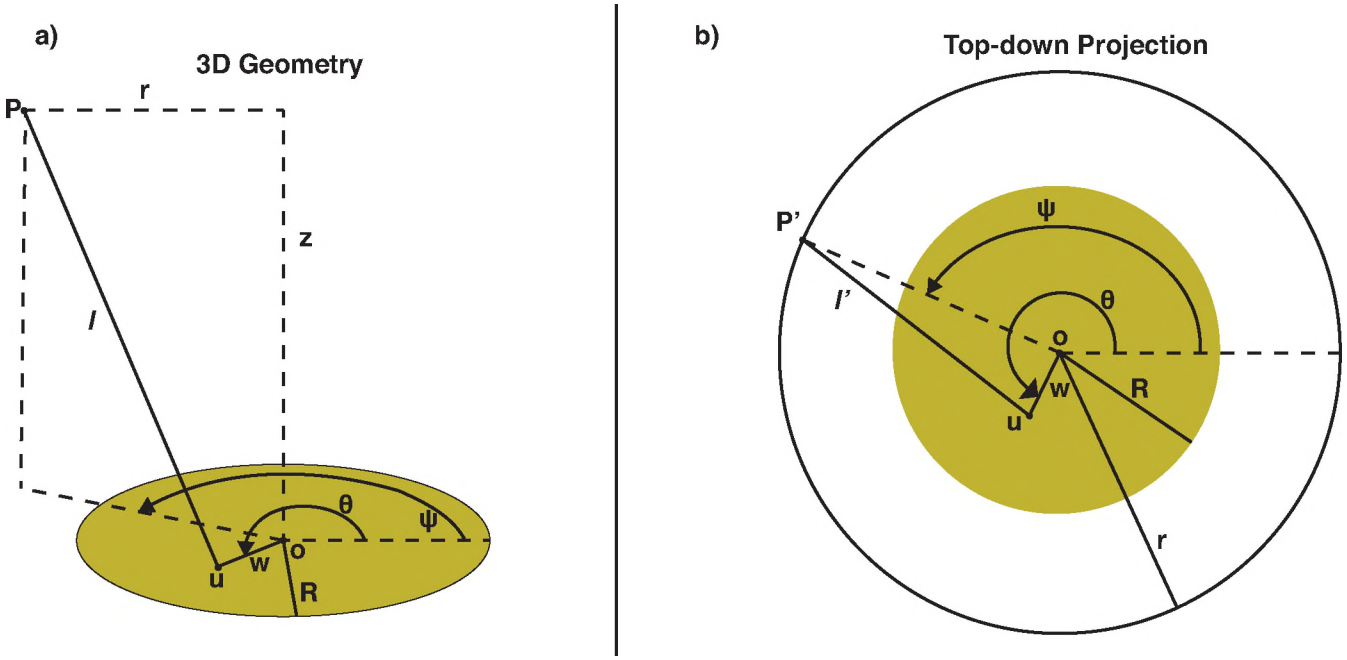

FIG. 1. a) The geometry of the path, l, between a point u on a finite disk of radius R and a point in space P. b) The projection of a) into the plane of the disk, which shows the geometry of a projected path length, l', between a point on the disk, u, and a point in the plane, P'.

disk, u, $\beta = \psi - \theta$, and r is the distance from o to P'.

Since, in a PI front, the radiation streams to the front, a larger average path length is equivalent to a later time when the PI front has traveled farther. For this reason, this article will refer to larger average path lengths as later in time because it suggests what the curvature of the front will be at the time it travels that distance. This assumes that the source does not change with time, but this is fine for the purpose of this work. It is also important to discuss the validity of this analysis at propagation distances less than one source radii. When the front is very close to the source, the average path length could be much larger than the minimum distance from the source to the front. One can resolve this issue by defining the source as multiple disks over the surface, since the approach taken here is normalized to the size of the source, with the size of the disk determined by a solid angle of the propagation medium that is reasonable for the system of interest. The PI front geometry would then be the sum of these wavefronts in a method analogous to Huygen's principle in optics, but this work investigates the front farther away from the source and will not discuss this point further.

$$\left\langle \frac{L}{R} \right\rangle = \frac{1}{\pi R^2} \int_0^R \int_0^{2\pi} w d\beta dw \frac{l}{R}. \tag{4}$$

Numerically integrating Equation 3, normalized to the source radius, over w and β provides the average path length, $\left\langle \frac{L}{R} \right\rangle$ in Equation 4, for a driving source with a cylindrically symmetric geometry in units of source radii. This averages over all of the path lengths from each point on the disk and results in path lengths that are always larger than the axial distance to the point. Using this result, the curvature in the Omega geometry reveals a smaller radius of curvature initially, that increases at larger average path lengths until it becomes almost infinite, as seen in Figure 2 a. This is reasonable because, for a system determined by geometry, as the front gets farther from the source it looks more like a point source. Figure 2 a shows that by about three source radii the front is relatively planar.

The curvature in the Z experiment geometry is different from the Omega case, as stated above, due to the more collimated nature of the source. Figure 2 b shows a larger radius of curvature starting very close to the source that becomes reasonably planar by an average path length of two source radii.

The curvature of a planar, supersonic Marshak wave evolves in time due to losses through walls that contain the propagation medium[29]. Ultimately, this is due to the radiation transport from the source being insufficient to support the Marshak wave against the energy losses through the walls. Figure 2 c compares the front curvature between the PI front results and the lowest order theory for Marshak waves using a modified diffusion coefficient of 0.46 mm^2 ns^{-1} and $\varepsilon = \frac{3}{4}\rho\kappa L(1-a) = 0.33$ with ρ the mass density, κ the opacity in cm^2 g^{-1}, L the source radius, and a the wall albedo, when the center of the fronts are at the same location.[29] These are the conditions that Hurricane and Hammer found their analytic model compared well with for a beryllium tube with a tantalum oxide foam.[29] This shows that the curvature between the two types of heat fronts is similar less than two source radii away. After the fronts reach two and a half source radii, the differences at the edge of the propagating medium show differences of a quarter of a source radii. For a source with a 500 μm radius, this corresponds to differences of about 125 μm near the edge of the container, which should be resolv-

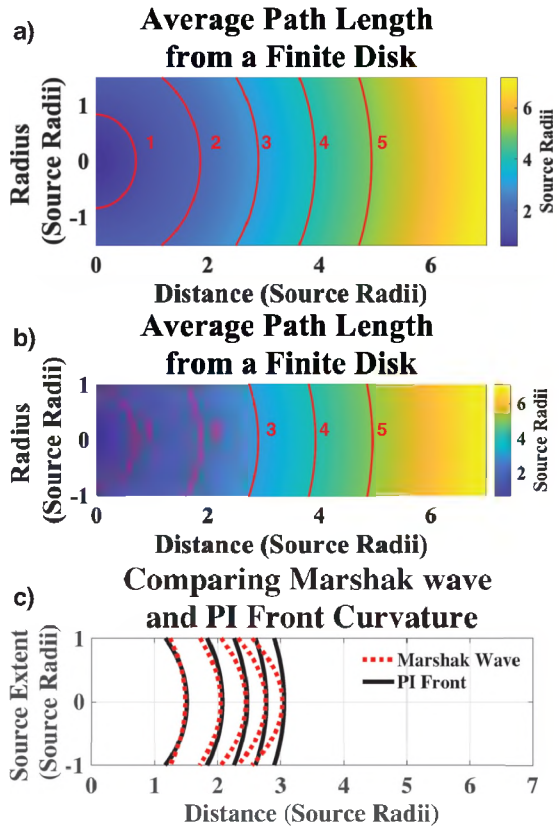

FIG. 2. The average path length from Equation 4 with a) showing the results for the Omega experiment and b) showing the relevant geometry for the experiment on Z. The red lines are contours showing average path lengths of one, two, three, four, and five source radii. c) A comparison between the PI front results from this work and the lowest order Marshak wave theory from Hurricane *et al.* using a modified diffusion coefficient of 0.46 $mm^2\ ns^{-1}$ and a wall coefficient of 0.33.[29] This shows that the curvature is similar until the front is about two source radii. Then, at about two and a half source radii away, the difference between the front positions reaches about one quarter of the source radius at the edge of the volume. This would be even more exaggerated in a smaller volume.

able with currently available imaging diagnostics. Since the model used here to determine the curvature of a PI front is purely geometric, it is necessary to discuss how the effects of wall losses may impact the validity of the above argument. The following will provide energy loss rate arguments for why these sorts of wall losses are not relevant to a PI front.

The work of Hurricane and Hammer[29] suggests that imperfectly reflecting walls provide the mechanism for evolving the supersonic Marshak wave curvature, which effectively amounts to an argument of the wall albedo being less than one. This means that the radiation transport produces the energy losses that account for the decrease in radius of curvature with time. There are more possible mechanisms for this energy loss, such as electron heat conduction through the walls of the tube, radiation-supported shock waves, and wall ablation. This work will focus on the effects of radiation transport and electron heat conduction in PI fronts.

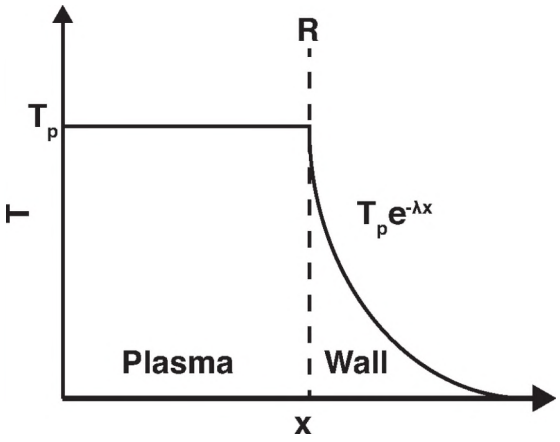

FIG. 3. The assumed temperature profile of the interaction between the post-front plasma and the container wall.

Considering the radiation transport through the container of the propagating medium for a PI front can be accomplished with a qualitative argument. Under the assumption that the walls are completely transparent, the radiation emitted from the post-front plasma escapes, which would lead to cooling. However, the physics of a PI front is such that the number of photoionization events far exceeds the recombination in the system and that the post-front region is transparent[3,15,21,22]. This means that the driving source will replenish any energy emitted from the plasma through the transparent walls faster than any loses that occur and that the radiation from the source that escapes through the walls is not necessary to support the front. Therefore, there are no concerns about radiation transport losses in the evolution of PI front curvature.

For electron heat conduction losses, this work will consider a section of the propagating medium container, with area A_w, in the post-front region and will use the Spitzer-Harm electron heat flux[34]. The heat flux will assume a constant temperature, T_P, in the post-front plasma and an exponential temperature profile, $T_w = T_0 e^{\lambda x}$, in the container wall with $T_0 = T_P$. Figure 3 shows a cartoon of the temperature profile used in this calculation. To show the importance of the electron heat conduction, this analysis will compare the energy losses through electron transport with radiation transport from the driving source through A_w. The ratio, $Q = \frac{\int dA_w Q_{SH}}{\int dE d\Omega dA B_E(T_S)}$, where Q_{SH} is the electron heat flux, E is the photon energy, $\Omega = \frac{A_w}{2\pi D}$ is the solid angle at a distance D in the hemisphere from the source, A is the area of the source, and $B_E(T)$ is the blackbody spectrum. Q is then,

$$Q = \frac{-A_w \frac{128}{2\pi m_e \nu_{ei}} c^2 n_e T \frac{dT}{dx}}{\frac{A_w}{2\pi D^2} \pi R^2 \sigma T_S^4}, \tag{5}$$

where m_e is the electron mass in eV, ν_{ei} is the electron-ion collision rate in s^{-1}, c is the speed of light in cm s^{-1}, n_e is the electron number density in cm^{-3}, T is the electron temperature in erg, $\frac{dT}{dx}$ is the temperature gradient in erg cm^{-1},

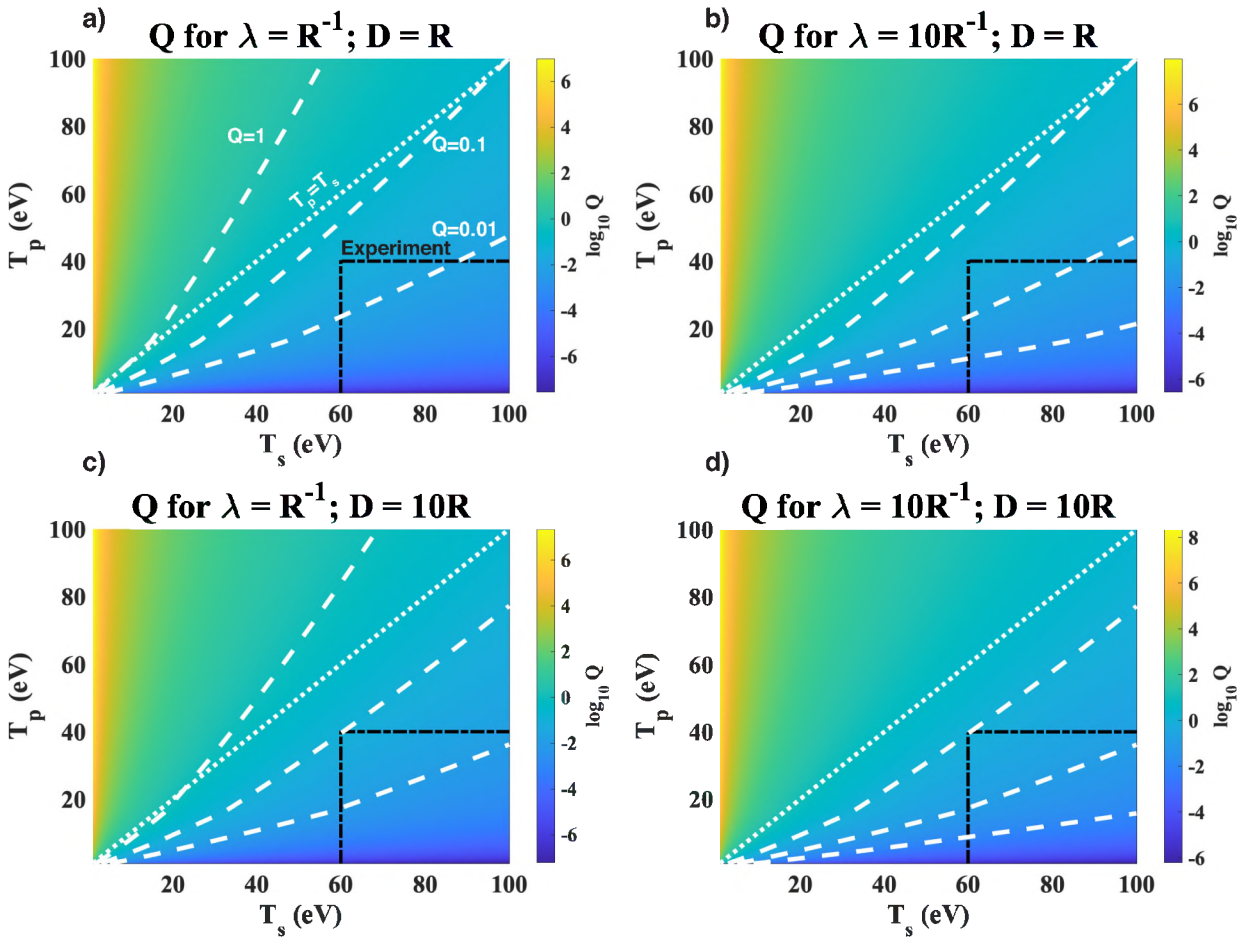

FIG. 4. The values of Q for the four permutations of the decay constant λ of the temperature profile in the wall and the distance, D, to the area of the container wall A_w with a) using $\lambda = \frac{1}{R}$; $D = R$, b) using $\lambda = \frac{10}{R}$; $D = R$, c) using $\lambda = \frac{1}{R}$; $D = 10R$, and d) using $\lambda = \frac{10}{R}$; $D = 10R$. a) has labels for all of the lines present in the figures with the white dotted line being where $T_p = T_s$ above which values are nonphysical, The black dot-dashed box shows expected experimental values, and the white dashed lines show where Q is 1, 0.1, and 0.01. To have a single point at each T_p, T_s pair in these figures, the calculation uses the maximum value of Q_{SH} for each temperature profile. The white dashed contours show where Q equals one and the energy losses through the walls from electron heat conduction are relevant to the radiation incident on the wall from the source. For a), b), and c) Q stays below one, and mostly below 0.1, for the conditions one would expect in an experiment[1,3,25], with the values above one occurring mostly occurring in the non-physical case when the plasma temperature exceeds the source temperature. d), the least favorable case indicates that wall loses due to electron heat fluxes start to approach expected experimental conditions ten source radii away when there are sharp temperature gradients in the wall suggesting that energy losses through the walls are generally not a concern in PI fronts and justifies the geometric model used to evaluate the front curvature.

σ is the Stefan-Boltzmann constant in units of erg s^{-1} cm^{-2} eV^{-4}, and T_S is the source temperature in eV. These calculations assume $n_e = 10^{23}$, $Z = 1$, and $R = 0.15$ cm in the wall with Z being the average ionization of the plasma to get an order of magnitude estimate of the electron heat flux. T_P and λ for the temperature profile in the wall parameterize Q_{SH}. To compare the effects of different wall materials, λ will take values of $\frac{1}{R}$ and $\frac{10}{R}$ to represent shallow and sharp temperature profiles in the wall, respectively. To see how increasing the distance from the source changes the effects of energy losses through the container from electron transport, D will take values of R and $10R$. The solid angle used for the radiation power through the container in Equation 5 is an order of magnitude estimate, which is fine for the goal of this argument and the rest of the assumptions made here. Figures 4 a, b, c, and d show Q for different values of T_S and T_P over all of the permutations of λ and D with $\lambda = \frac{1}{R}$ and $D = R$, $\lambda = \frac{10}{R}$ and $D = R$, using $\lambda = \frac{1}{R}$ and $D = 10R$, and $\lambda = \frac{10}{R}$ and $D = 10R$ respectively. The white dashed contours in Figures 4 a, b, c, and d indicate where Q is 1, 0.1, and 0.01, the white dotted line shows where $T_p = T_s$, and the black dot-dashed lines show where an experiment might exist. The regions where the ratio exceeds one are mostly constrained to where the source temperature is below the plasma temperature, below the dotted line, which is not physical and not a concern for an experiment. The source temperatures for these experiments will be larger than 60 eV with plasma temperatures below about 40 eV and will occupy the lower right corner of the parameter

space in Figure 4 inside the black box.[1,3,22,25] This shows that there is a region with electron heat fluxes are below 10% of the radiation energy fluxes for any of the four values of R and λ shown here. There are only concerns about effects on the wall curvature due to electron heat fluxes when there are sharp temperature gradients in the container wall, as in Figures 4 b and d. These results suggest that one should design an experiment with shallow temperature gradients into the wall and low plasma temperatures in order to ignore the effects of electron heat conduction on the front curvature.

These results indicate possible measurement techniques to identify PI fronts and some aspects of the target design to consider in an experiment.

The main takeaway is that it is possible to distinguish a PI front from a supersonic Marshak wave, or any supersonic nonlinear radiation diffusion wave, through the evolution of the front curvature with time. Due to the lack of significant wall loses in a PI front, the radius of curvature increases as the front propagates away from the source, in a planar geometry, which is the opposite of a planar Marshak wave. A comparison of the geometric model of a PI front with an analytic model of a Marshak wave from the literature shows differences of greater than 100 μm for a 1 mm diameter source at distances of three source radii. This suggests that existing imaging diagnostics can provide insight into the heat front physics in an experiment and identify signatures of a PI front. There are also potential spectral signatures due to this curvature. The flattening of a PI front will reduce the volume of cool material in a probe volume as an experiment probes farther from the source, which means that changing the distance from the source of an emission or absorption measurement would detect a decrease in the line structure from lower ionization states. These are powerful tools for evaluating the physics in a heat front experiment.

Additionally, it is important to consider the effects of the container on the heat front. Since the radiation transport is not a significant energy loss mechanism for a PI front, a container with a large albedo may affect the evolution of the front. If the container is able to re-emit a large fraction of the incident radiation it could have a significant effect on the front itself because the post-front region becomes so transparent. This would change the geometry of the problem and one would need to consider two, extended sources driving the PI front. For this reason, it would be useful to build a target for the experiment out of a low-Z material so that it does not re-emit a significant fraction of the source radiation after the front passes. This material choice would also increase the wall losses in a Marshak wave and exaggerate the differences in curvature with a PI front. This article describes a geometric model for the curvature of a PI front and notes the differences when compared with the literature on the curvature of a Marshak wave. The increase in radius of curvature with time in a PI front is the opposite of a Marshak wave, in planar geometry, which is a useful diagnostic tool for any PI front experiment. An analysis of the wall losses show that they are negligible compared to the energy input from the driving source and justifies the use of a geometric model for the front curvature. These results suggest a powerful method for evaluating the physics in a heat front experiment and suggest material choices for a PI front target that will reduce the complexity of the data analysis.

ACKNOWLEDGMENTS

This material is based upon work supported by the National Science Foundation MPS-Ascend Postdoctoral Research Fellowship under Grant No. 2138109. This work is funded by the U.S. Department of Energy NNSA Center of Excellence under cooperative agreement number DE-NA0003869.

AUTHOR DECLARATIONS

The authors have no conflicts to disclose.

DATA AVAILABILITY STATEMENT

The data that support the findings of this study are available from the corresponding author upon reasonable request.

[1] R. C. Mancini, T. E. Lockard, D. C. Mayes, I. M. Hall, G. P. Loisel, J. E. Bailey, G. A. Rochau, J. Abdallah, I. E. Golovkin, and D. Liedahl, "X-ray heating and electron temperature of laboratory photoionized plasmas," Phys. Rev. E **101**, 051201 (2020).

[2] G. P. Loisel, J. E. Bailey, D. A. Liedahl, C. J. Fontes, T. R. Kallman, T. Nagayama, S. B. Hansen, G. A. Rochau, R. C. Mancini, and R. W. Lee, "Benchmark experiment for photoionized plasma emission from accretion-powered x-ray sources," Phys. Rev. Lett. **119**, 075001 (2017).

[3] H. J. LeFevre, M. Springstead, K. Kelso, R. C. Mancini, G. P. Loisel, P. A. Keiter, R. P. Drake, and C. C. Kuranz, "The design of a photoionization front experiment using the z-machine as a driving source and estimated measurements," Physics of Plasmas **28**, 093304 (2021), https://doi.org/10.1063/5.0049527.

[4] G. A. Rochau, J. E. Bailey, R. E. Falcon, G. P. Loisel, T. Nagayama, R. C. Mancini, I. Hall, D. E. Winget, M. H. Montgomery, and D. A. Liedahl, "Zapp: The z astrophysical plasma properties collaboration," Physics of Plasmas **21**, 056308 (2014), https://doi.org/10.1063/1.4875330.

[5] R. C. Mancini, J. E. Bailey, J. F. Hawley, T. Kallman, M. Witthoeft, S. J. Rose, and H. Takabe, "Accretion disk dynamics, photoionized plasmas, and stellar opacities," Physics of Plasmas **16**, 041001 (2009), https://doi.org/10.1063/1.3101819.

[6] M. Fraser, "Supernovae and transients with circumstellar interaction," Royal Society Open Science **7**, 200467 (2020), https://royalsocietypublishing.org/doi/pdf/10.1098/rsos.200467.

[7] C. S. Kochanek, "The physics of flash (supernova) spectroscopy," Monthly Notices of the Royal Astronomical Society **483**, 3762–3772 (2018), https://academic.oup.com/mnras/article-pdf/483/3/3762/27303694/sty3363.pdf.

[8] D. A. Liedahl, "X-ray photoionized plasmas in space and in the laboratory," Astrophysics and Space Science **336**, 251–256 (2011).

[9] R. A. Chevalier and C. M. Irwin, "X-RAYS FROM SUPERNOVA SHOCKS IN DENSE MASS LOSS," The Astrophysical Journal **747**, L17 (2012).

[10] B. E. Robertson, R. S. Ellis, J. S. Dunlop, R. J. McLure, and D. P. Stark, "Early star-forming galaxies and the reionization of the universe," Nature **468**, 49–55 (2010).

[11] Schaerer, D. and de Barros, S., "The impact of nebular emission on the ages of z{\sf\approx} 6 galaxies," A&A **502**, 423–426 (2009).

[12] de Barros, S., Schaerer, D., and Stark, D. P., "Properties of z 3-6 lyman break galaxies - ii. impact of nebular emission at high redshift," A&A **563**, A81 (2014).

[13] Schaerer, D. and de Barros, S., "On the physical properties of z -8 galaxies," A&A **515**, A73 (2010).

[14] E. Chatzopoulos, J. C. Wheeler, J. Vinko, R. Quimby, E. L. Robinson, A. A. Miller, R. J. Foley, D. A. Perley, F. Yuan, C. Akerlof, and J. S. Bloom, "SN 2008am: A SUPER-LUMINOUS TYPE IIn SUPERNOVA," The Astrophysical Journal **729**, 143 (2011).

[15] R. P. Drake, G. Hazak, P. A. Keiter, J. S. Davis, C. R. Patterson, A. Frank, E. G. Blackman, and M. Busquet, "DESIGN OF LABORATORY EXPERIMENTS TO STUDY PHOTOIONIZATION FRONTS DRIVEN BY THERMAL SOURCES," The Astrophysical Journal **833**, 249 (2016).

[16] B. Strömgren, "The Physical State of Interstellar Hydrogen." The Astrophysical Journal **89**, 526 (1939).

[17] F. A. Goldsworthy, "On the propagation and structure of ionization fronts," Rev. Mod. Phys. **30**, 1062–1068 (1958).

[18] F. A. Goldsworthy and M. J. Lighthill, "Ionization fronts in interstellar gas and the expansion of hii regions," Philosophical Transactions of the Royal Society of London. Series A, Mathematical and Physical Sciences **253**, 277–300 (1961), https://royalsocietypublishing.org/doi/pdf/10.1098/rsta.1961.0001.

[19] F. D. Kahn, "The acceleration of interstellar clouds," Bulletin of the Astronomical Institutes of the Netherlands **12**, 187 (1954).

[20] W. I. Axford and M. J. Lighthill, "Ionization front in interstellar gas: The structure of ionization fronts," Philosophical Transactions of the Royal Society of London. Series A, Mathematical and Physical Sciences **253**, 301–333 (1961), https://royalsocietypublishing.org/doi/pdf/10.1098/rsta.1961.0002.

[21] W. J. Gray, P. A. Keiter, H. Lefevre, C. R. Patterson, J. S. Davis, B. van Der Holst, K. G. Powell, and R. P. Drake, "Laboratory photoionization fronts in nitrogen gas: A numerical feasibility and parameter study," The Astrophysical Journal **858**, 22 (2018).

[22] W. J. Gray, P. A. Keiter, H. Lefevre, C. R. Patterson, J. S. Davis, K. G. Powell, C. C. Kuranz, and R. P. Drake, "Atomic modeling of photoionization fronts in nitrogen gas," Physics of Plasmas **26**, 052901 (2019), https://doi.org/10.1063/1.5090803.

[23] T. R. Boehly, R. S. Craxton, T. H. Hinterman, J. H. Kelly, T. J. Kessler, S. A. Kumpan, S. A. Letzring, R. L. McCrory, S. F. B. Morse, W. Seka, S. Skupsky, J. M. Soures, and C. P. Verdon, "The upgrade to the omega laser system," Review of Scientific Instruments **66**, 508–510 (1995), https://doi.org/10.1063/1.1146333.

[24] J. S. Davis, Y. Frank, E. Raicher, M. Fraenkel, P. A. Keiter, S. R. Klein, R. P. Drake, and D. Shvarts, "Measurements of laser generated soft x-ray emission from irradiated gold foils," Review of Scientific Instruments **87**, 11D609 (2016), https://aip.scitation.org/doi/pdf/10.1063/1.4960816.

[25] J. S. Davis, R. P. Drake, M. Fraenkel, Y. Frank, P. A. Keiter, S. R. Klein, E. Raicher, D. Shvarts, and M. R. Trantham, "Soft x-ray emission from laser-irradiated gold foils," Physics of Plasmas **25**, 073304 (2018), https://doi.org/10.1063/1.5036934.

[26] R. E. Marshak, "Effect of radiation on shock wave behavior," The Physics of Fluids **1**, 24–29 (1958), https://aip.scitation.org/doi/pdf/10.1063/1.1724332.

[27] C. A. Back, J. D. Bauer, O. L. Landen, R. E. Turner, B. F. Lasinski, J. H. Hammer, M. D. Rosen, L. J. Suter, and W. H. Hsing, "Detailed measurements of a diffusive supersonic wave in a radiatively heated foam," Phys. Rev. Lett. **84**, 274–277 (2000).

[28] C. A. Back, J. D. Bauer, J. H. Hammer, B. F. Lasinski, R. E. Turner, P. W. Rambo, O. L. Landen, L. J. Suter, M. D. Rosen, and W. W. Hsing, "Diffusive, supersonic x-ray transport in radiatively heated foam cylinders," Physics of Plasmas **7**, 2126–2134 (2000), https://doi.org/10.1063/1.874057.

[29] O. A. Hurricane and J. H. Hammer, "Bent marshak waves," Physics of Plasmas **13**, 113303 (2006), https://doi.org/10.1063/1.2388268.

[30] P. A. Keiter, G. A. Kyrala, R. G. Watt, G. C. Idzorek, R. R. Peterson, B. Wood, P. Adams, R. E. Chrien, D. Peterson, and M. Wood-Schultz, "Preliminary results from an astrophysically relevant radiation transfer experiment," in *High Energy Density Laboratory Astrophysics* (Springer Netherlands, Dordrecht, 2005) pp. 163–170.

[31] P. Keiter, M. Gunderson, J. Foster, P. Rosen, A. Comley, M. Taylor, and T. Perry, "Radiation transport in inhomogeneous media," Physics of Plasmas **15**, 056901 (2008), https://doi.org/10.1063/1.2927529.

[32] A. P. Cohen and S. I. Heizler, "Modeling of supersonic radiative marshak waves using simple models and advanced simulations," Journal of Computational and Theoretical Transport **47**, 378–399 (2018), https://doi.org/10.1080/23324309.2018.1489846.

[33] A. P. Cohen, G. Malamud, and S. I. Heizler, "Key to understanding supersonic radiative marshak waves using simple models and advanced simulations," Phys. Rev. Research **2**, 023007 (2020).

[34] R. Drake, *High-Energy-Density Physics: Foundation of Inertial Fusion and Experimental Astrophysics*, Graduate Texts in Physics (Springer International Publishing, 2018).